Russian Journal of Earth Sciences

On the Dynamics of Floating Plastic Debris Under the Action of Waves on the Sea Surface. Numerical Modeling

G. E. Khazanov[*,1] **and S. A. Ermakov**[1,2]

[1]Federal Research Center A. V. Gaponov-Grekhov Institute of Applied Physics of the Russian Academy of Sciences, Nizhny Novgorod, Russia
[2]Volga State University of Water Transport, Nizhny Novgorod, Russia
* **Correspondence to:** Gregory Khazanov, g.khazanov@ipfran.ru

Abstract: Ocean plastic pollution poses a serious environmental threat to both natural ecosystems and human health. An important field of research on this problem is the development of the physical foundations and methods of remote sensing of plastic debris (PD). The plastic in the ocean and inland waters is largely associated with buoyant polyethylene (PE) films, which are expected to be located the water surface. However, everyday observations show that plastic objects, including PE films, are partially or completely submerged in the near-surface water layer, even though the density of these fragments is lower than that of water. This makes detecting plastic pollution using radar methods more challenging than might be expected. This paper is focused on numerical modeling of an initial stage of the dynamics of a buoyant plastic film placed on the water surface when an intense gravity-capillary wave (GCW) approaches the film. The modeling is performed using the open-source software “OpenFOAM”. It has been revealed that for a highly nonlinear GCW with a bulge structure near the wave crest, there is an “overflow” of water over the film with subsequent sinking of its edge. It has also been obtained that a buoyant PE film sank below the water surface rises slower in the presence of GCW than in the “no wave” case. The explanation of the film immersion effect is given based on the hypothesis that an averaged hydrodynamic force directed against the Archimedean force arises in the field of the orbital wave motions of the liquid particles.

Keywords: Plastic debris in water, polyethylene films, gravity-capillary waves, remote sensing.

Citation: Khazanov G. E. and Ermakov S. A. (2026), On the Dynamics of Floating Plastic Debris Under the Action of Waves on the Sea Surface. Numerical Modeling, *Russian Journal of Earth Sciences*, 26, ES1002, EDN: LWEBTI, https://doi.org/10.2205/2026es001093

Research Article

Received: October 28, 2025
Accepted: December 3, 2025
Published: January 29, 2026

1. Introduction

Plastic pollution of the ocean and inland water bodies is currently a serious environmental threat [see, e.g., *Andrady*, 2011; *Chubarenko et al.*, 2020; *Cózar et al.*, 2014; *Suaria et al.*, 2023]. An important field of research on this problem is the development of the physical principles and methods of remote sensing of plastic debris (PD), primarily using aerospace instruments for monitoring the aquatic environment [see, *Hu*, 2021; *Simpson et al.*, 2022, and references therein]. Microwave radar is one of the most perspective and widely used instruments which operates in all-weather and day-and-night conditions and which can be used for PD detection [*Simpson et al.*, 2022]. Until recently, most of the research has focused on micro plastics, which are particles with dimensions of a few millimeters or smaller. Biogenic surfactant films on the water surface, arising as a result of the life activity of microalgae inhabiting plastic particles, were considered as one of the main physical mechanisms of microplastic manifestations in the signals of remote ocean observation systems, [*Harrison et al.*, 2018; *Smith et al.*, 2021]. The biogenic surfactant films cause partial suppression of wind gravity-capillary waves (GCW) due to an increase in the GCW damping coefficient [see, *Ermakov and Khazanov*, 2022, and references therein], which leads to the formation of “smoothed” areas on the water surface – so-called slicks

[*Phillips*, 1977] displayed on satellite radar panoramas of the ocean [*Davaasuren et al.*, 2018; *Evans and Ruf*, 2022; *Sun et al.*, 2023].

Note, that the biofilms are formed also on larger-scale PD fragments (macro plastic): polyethylene (PE) bags, pieces of PE film, food plastic containers, etc. [see, e.g., *Sapozhnikov et al.*, 2023; *Vodeneeva et al.*, 2024, and references therein], and can be considered as one of the indicators of macro plastic, too. When analyzing the factors that determine the possibilities of microwave probing of macro PD, along with the biofilms, it is necessary to consider direct scattering of electromagnetic waves on plastic fragments floating on the water surface, as well as the influence of these fragments on small-scale wind waves [*Arii et al.*, 2014; *Simpson et al.*, 2023]. Here, it should be mentioned that plastic objects, as it follows from everyday observations, are partially or completely submerged in the near-surface water layer, even if the density of these fragments is less than the water density (see, for example, Whale shark and plastic bag). Since microwave radiation practically cannot penetrate below the sea surface, this makes detecting plastic pollution using radar methods more challenging than might be expected.

Another aspect of this problem is related to the fact that plastic fragments in the near-surface layer form small ripples on the water surface [*Ermakov et al.*, 2024], which affects the radar scattering signal and can both distort the resulting picture and serve as an indicator of the presence of PD fragments in the near-surface layer. To analyze the radar signal in the presence of such ripples on the surface, it is necessary to study the physical mechanisms and dynamics of plastic objects in the near-surface layer, which is currently insufficiently studied.

Sinking of plastic objects from the water surface to the subsurface layer is believed to be associated with wind mixing [*Forsberg et al.*, 2020; *Kukulka et al.*, 2012], convergent currents, wind waves, particularly wave breakers [*Forsberg et al.*, 2020], but these mechanisms have not been well studied yet. Recently, a new effect of sinking of a floating PE films, initially placed under the water surface, due to the action of surface waves have been revealed in [*Khazanov and Ermakov*, 2025]. The effect was obtained from numerical modeling of the dynamics of the floating film in the field of surface waves using the open-source software “OpenFOAM”. However, the question of how the floating film can leave the water surface due to surface waves remained open. Studying these issues is very important both from a fundamental point of view and for solving applied problems of detecting and mapping areas covered by PD fragments.

One should note that problems of hydrodynamic flow around bodies are, in general, very complex, so a large number of works have been devoted to the development and testing of numerical methods for solving such problems, in particular, in the OpenFOAM environment. A significant number of model experiments on the fluid-solid interaction, deformable structures, including in the presence of a water-air interface, have shown good results and proven the suitability of this package for solving a wide class of similar problems [see, e.g., *Brown et al.*, 2022; *Hron and Turek*, 2006].

This paper is focused on numerical modeling of the initial stage of the dynamics of a floating plastic film placed on the water surface when intense gravity-capillary waves approach the film. It has been shown that, despite the positive buoyancy, the film in the presence of water waves can either float or sink being in equilibrium at a certain depth.

The paper is organized as follows. First the basic equations and boundary conditions as well as the geometric scheme of the numerical experiment and a computational grid are presented. Then the results of modeling of GCW of small and large amplitudes in the absence of a PE film are described. After that the dynamics of a PE film initially located under the water surface for the “no wave” case is modeled. Finally, the results for PE film located on the water surface in the presence of GCW of different amplitudes are presented and discussed.

2. Governing Equations and Numerical Methods

The numerical modeling was performed using the open-source software OpenFOAM. A large number of studies were devoted to the development and testing of numerical methods to describe hydrodynamic flows around bodies, particularly in the OpenFOAM package. A significant number of model experiments on the fluid-solid interaction, deformable structures, including the presence of an air-water interface, showed good results and proved the suitability of this package for solving a wide class of such problems [*Brown et al.*, 2022; *Hron and Turek*, 2006; *Tuković et al.*, 2018]. One of the main advantages of this package for scientific purposes is the availability of open source code. In the OpenFOAM there is a set of tools "`solids4foam`" [*Cardiff et al.*, 2018; *Tuković et al.*, 2018] for the problems of interaction of a fluid and solid bodies, including those with different elasticity. Different approaches were used in various works to model numerically such processes. A common feature of all approaches was the difference in the coordinate systems used to describe dynamics in different media: the equations of solid mechanics are formulated in Lagrangian variables, while the equations of fluid dynamics are traditionally written in a fixed Eulerian system. This work uses the so-called Arbitrary Lagrangian Eulerian (ALE) approach [*Donea et al.*, 2004], which allows the grid topology to either remain fixed or move with the Lagrangian particles.

It should be noted that the "ALE" technique demonstrates good results, especially for maintaining a high-quality grid near the interface, which leads to more accurate calculations of the fluid dynamics in this region [*Tezduyar et al.*, 2010]. The solid body equations are solved using a Lagrangian approach, while the motion of fluid particles is considered using an Euler approach on a "moving grid". It should also be noted that this package uses a two-domain approach, dividing the computational domain into two regions: the fluid and the solid body, and sequentially calculating their dynamics separately, taking into account the interaction between them due to the boundary conditions.

2.1. Governing Equations

The fluid is described as incompressible and Newtonian. A two-dimensional problem is considered in the XZ plane, where the OX axis is directed along the wave propagation, the OZ axis is directed vertically upwards. The governing equations of hydrodynamics – the continuity equation and the Navier–Stokes equation are written as:

$$\nabla \mathbf{v} = 0,$$

$$\frac{\partial \mathbf{v}}{\partial t} + ((\mathbf{v} - \mathbf{v}_m) \cdot \nabla)\mathbf{v} = \nu \Delta \mathbf{v} - \frac{1}{\rho}\nabla p + \mathbf{g}.$$

Here ρ – fluid density, $\mathbf{v}$ – fluid velocity, p – fluid pressure, $\mathbf{g} = (\mathbf{0}, -g_\mathbf{z})$ here g_z – acceleration due to gravity, ν – kinematic viscosity, $\mathbf{v}_m$ – the velocity of the reference frame (the mesh velocity in the "ALE" method) that is required to deform the fluid mesh to account for the structural deformation of the solid.

An additional restriction for the "ALE" approach is that the grid velocity must satisfy the geometric conservation law [*Thomas and Lombard*, 1979].

$$\frac{\partial V^{\mathrm{ce}}}{\partial t} + \nabla \cdot v_m = 0.$$

Here, V^{ce}- dimensionless control volume (cell volume). This condition requires that the change in volume of each control volume between two adjacent time steps is equal to the volume by which the cell boundary has moved during the time step.

The volume of fluid method ("VOF") was used to track the free surface elevation [*Jasak*, 1996]. Two immiscible phases (air and water) are treated as one effective fluid that is modeled simultaneously throughout the entire computational domain with the α – function determining the fraction of the specific fluid that exists in each cell and serving as an identifier for the location of the water-air interface. The equation for the volume fraction α is:

$$\frac{\partial \alpha}{\partial t} + \nabla \cdot (\alpha v) = 0,$$

where α – the volume fraction of water in the cell, which varies from 0 to 1 (the cell is completely filled with water or air, respectively). A value of 0.5 approximately corresponds to the air-water interface. The local density and viscosity of the combined fluid in each cell are determined as: $\rho = \alpha \rho_{\text{water}} + (1-\alpha)\rho_{\text{air}}$, $\mu = \alpha \mu_{\text{water}} + (1-\alpha)\mu_{\text{air}}$.

To model the surface wave, the first-order Stokes wave was used with the “`waves2foam`” module [*Dean and Dalrymple*, 1991; *Higuera et al.*, 2013]. The free surface elevation within this model is described as:

$$\eta(x,t) = a\cos(kx - \omega t). \tag{1}$$

Here k denotes the wave number, ω the wave frequency, and a – the wave amplitude. The dispersion equation of gravity-capillary waves is

$$\omega^2 = kg \cdot \tanh(kH) \cdot \{1 + o(ka)^2\}, \tag{2}$$

where H is the water depth.

The solid structure of the PE film is described as elastic, and the equation that defines its deformation is the law of momentum conservation in the Lagrangian system for the deformation vector $\mathbf{u}$:

$$\rho \frac{\partial^2 \mathbf{u}}{\partial t^2} = \nabla \sigma + \rho \mathbf{g}. \tag{3}$$

Here, ρ is the solid density, $\mathbf{u}$ the displacement vector, $\boldsymbol{\sigma}$ the Cauchy stress tensor. In this case, we are dealing with sufficiently large and arbitrary deformations of the body. It means that the changes in the volume area or orientation of the control volume are not small during the simulation. That is why the simplified linear model cannot be applied. Therefore, we use a nonlinear model, the finite strain method. In this case, the material is defined by specifying the Cauchy stress tensor:

$$\sigma = \frac{1}{J}\mathbf{F} \cdot \sum \cdot \mathbf{F}^T,$$

$$\mathbf{F} = \mathbf{I} + (\nabla_{\mathbf{0}} \mathbf{u})^T,$$

$\mathbf{F}$ – the deformation gradient tensor, representing the difference between the initial and deformed states of the material [see, *Ciarlet*, 1988]. $J = \det[\mathbf{F}]$ – the Jacobian matrix, $\mathbf{I}$ – is the unit tensor, $\sum$ – is the second Piola–Kirchhoff stress tensor. To account finite strains, the St. Venant–Kirchhoff constitutive material model is used, and the $\sum$ can be written as:

$$\sum = 2\mu^{\mathbf{s}}\mathbf{E} + \lambda \operatorname{tr}(\mathbf{E})\mathbf{I},$$

$$\sigma = \frac{1}{J}\mathbf{F}[2\mu^{\mathbf{s}}\mathbf{E} + \lambda \operatorname{tr}(\mathbf{E})\mathbf{I}]\mathbf{F}^T,$$

$\mu^{\mathbf{s}}$ and λ – the Lame parameters, $\mathbf{E}$ – the Green–Lagrange strain tensor

$$\mathbf{E} = \frac{1}{2}\left(\mathbf{F}^T\mathbf{F} - \mathbf{I}\right).$$

The Lame parameters $\mu^{\mathbf{s}}$ and λ related to the material properties as Poisson’s ratio μ and the Young’s modulus E_s as:

$$\mu^{\mathbf{s}} = \frac{E_s}{2(1+\mu)},$$

$$\lambda = \frac{\mu E_s}{(1+\mu)(1-\mu)}.$$

The Poisson's ratio μ and the Young's modulus E_s determine the elastic properties of the material in this problem.

2.2. Boundary Conditions

The kinematic boundary condition is that the velocity must be continuous at the interface between the liquid and the solid. From the equation of momentum conservation, we can derive the dynamic boundary condition that requires the forces to be equal along the normal to the interface. These conditions can be expressed as follows:

$$\mathbf{v}^{\mathrm{i}}_{\mathrm{fluid}}=\mathbf{v}^{\mathrm{i}}_{\mathrm{solid}}, \tag{4}$$

$$\mathbf{n}^{\mathrm{i}}\sigma^{\mathrm{i}}_{\mathrm{fluid}}=\mathbf{n}^{\mathrm{i}}\sigma^{\mathrm{i}}_{\mathrm{solid}}, \tag{5}$$

where n is the unit normal vector to the interface, and "i" runs over all phases of the solid – water interface.

The bottom and the right boundary of the computational domain were assumed to be solid walls, on which the "no slip" condition was set (the index f_b denotes the lower, f_r the right, f_a the upper, and f_l the left boundaries of the computational domain):

$$v_{f_{b,r}} = 0.$$

At the distance of about one wavelength before the right boundary of the domain, a surface wave absorption condition was imposed to prevent reflection. For more information of the wave generation and absorption technique, [see, e.g., *Dean and Dalrymple*, 1991; *Higuera et al.*, 2013].

At the upper boundary, the air pressure was assumed to be equal to the atmospheric pressure.

$$p_{f_a} = p_0.$$

Here p_0 – the atmospheric pressure.

A surface wave was set up in a region of the order of one wavelength near the left boundary of the domain. The velocity at the left boundary was taken to be equal to the velocity in the wave. This condition can be written as:

$$v_{f_l}(z) \approx U_0 \exp(kz).$$

Here U_0 is the orbital velocity on the water surface, which can be calculated based on equations (1, 2) by specifying the period and amplitude of the wave.

To enforce these interface conditions a strongly-coupled Dirichlet–Neumann coupling algorithm is used [*Widlund*, 1988], which involves applying the Dirichlet condition in the fluid region to determine the velocity at the interface between the two regions, and using the Neumann condition to determine the force at the interface in the solid region, as described in equations (4) and (5). The calculation algorithm works as follows: the calculation in the fluid region determines the force at the interface and passes this information to the solid body solver, which in turn passes the displacements at the interface to the fluid grid solver. After that, the grid in the fluid region moves and updates, and this happens again at each time step. While the grid in the fluid region changes over time due to the deformation of the fluid-solid interface, the grid in the solid region always remains in its initial configuration due to the use of the Lagrangian approach. Fluid mesh deformation is performed using the Laplace equation of mesh motion with variable diffusion [*Tuković and Jasak*, 2012].

2.3. Geometric Scheme of the Experiment

Numerical calculations were performed for a 2D problem, and the computational domain was constructed with dimensions of 2 m along the x-axis and 35 cm along the z-axis. The surface wave propagated from left to right along the x-axis, as shown in Figure 1. The wavelength was 40 cm, and the wave steepness varied from $ka = 0.18$ to 0.33. Water depth was 18 cm. The water viscosity was 0.01 cm^2/s. The PE film length varied from 20 to 80 cm, the thickness was 0.4 mm, the Poisson's ratio was 0.3, and the elasticity of the PE imitator E_s varied from 2×10^7 to 2×10^8 Pa. The density of the PE imitator was 0.9 g/m^3. The geometric scheme of the numerical experiment is presented in Figure 1.

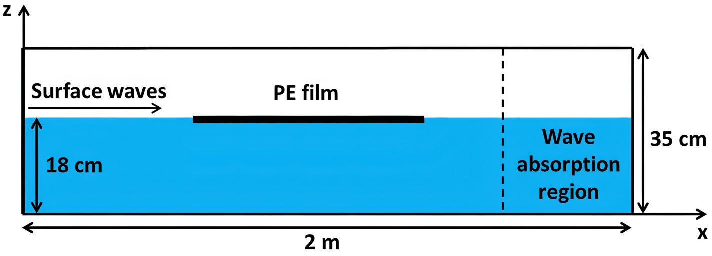

Figure 1. Geometric scheme of a numerical experiment.

The computational domain is divided into a finite number of convex polyhedral control volumes or cells, which are bounded by convex polygons. The cells do not overlap and completely fill the spatial domain. Second-order difference schemes are used for spatial and temporal discretization of the equations. The number of cells in different simulations ranged from 100,000 to 300,000 in various simulations due to the convergence analysis, which showed no significant changes in physical quantities when the grid was further refined. The highest cell density is achieved near the body, where the grid resolution reaches $dx = 0.003$ cm, $dz = 0.004$ cm. The initial time step was $dt = 0.00001$ s and was modified during the simulation based on the maximum Courant number $Co = 0.25$, with an additional constraint on the maximum time step $dt < 0.0001$ s to ensure the stability of the numerical schemes. An example of the computational grid at an initial moment ($t = 0$) and after switching the wave on is shown in Figure 2.

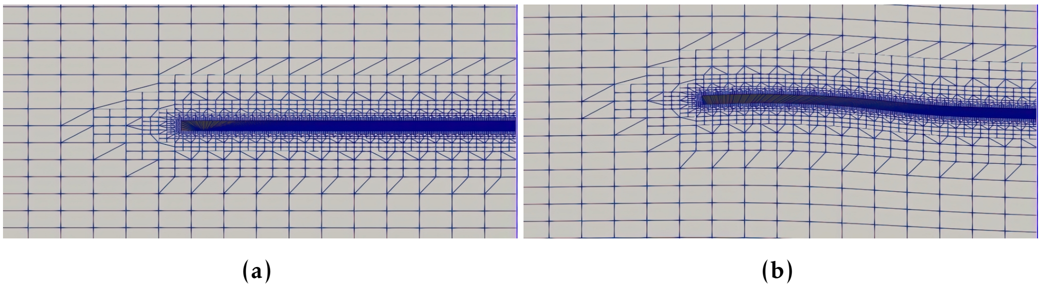
(a) (b)

Figure 2. A computational grid around the film for $t = 0$ s (a) and $t = 0.45$ s (b).

In Figure 2 one can see an example of how the grid in the fluid region adapts to the body's displacements, which are caused by the force exerted on the body by the fluid. Despite the significant displacements, the grid remains well-defined in terms of its main characteristics, such as orthogonality, skewness, and the aspect ratio. This allows for accurate calculation of dynamic properties in the fluid during the simulation, including the area near the water-film interface.

3. Results

3.1. GCW on clean water

3.1.1. Small amplitude GCW

For the first-order Stokes surface wave which is set at the left boundary, the orbital velocity should decay exponentially with depth as $v(z) \approx U_0 \exp(kz)$. Here U_0 is the wave orbital velocity on the water surface $z = 0$. A comparison of the orbital velocity profile obtained in a numerical calculation with theory is shown in Figure 3.

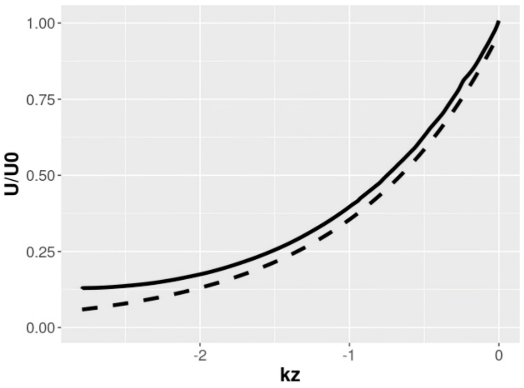

Figure 3. Comparison of the theoretical (solid line) and numerical (dotted line) normalized orbital velocity profiles as a function of normalized depth.

The surface elevation profile ξ, of a small amplitude GCW with the steepness of $ka \sim 0.21$ is shown in Figure 4, thus demonstrating, that the profile is slightly asymmetric, but is far from breaking.

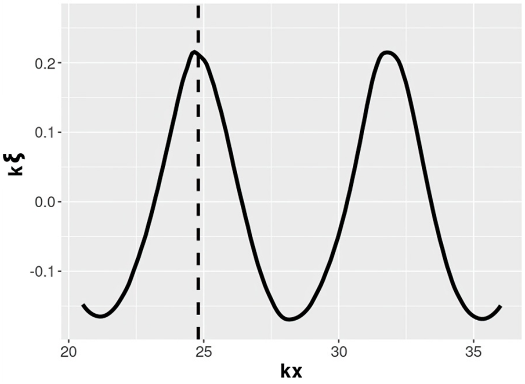

Figure 4. Dimensionless profile of a small amplitude surface GCW ($ka \sim 0.21$) as a function of dimensionless coordinate kx.

3.1.2. Steep GCW

The profile of highly nonlinear GCW with slopes close to the breaking condition ($ka \sim 0.28$–0.33) is shown in Figure 5.

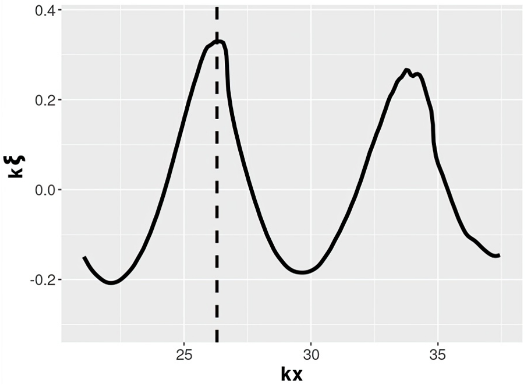

Figure 5. Same as Figure 4 for a large amplitude surface GCW ($ka \sim 0.33$).

As it follows from Figure 5 the GCW profile is characterized by the presence of a bulge-like structure in the vicinity of the wave crest, which is typical for GCW with lengths of about 30–40 cm and less and which can be described as “micro-breaking” [*Duncan*, 2001; *Ermakov et al.*, 2022; *Qiao and Duncan*, 2001; *Rapp and Melville*, 1990]. One should remind that apart from the bulge structures, the so-called parasitic capillary ripples in the mm wavelength range can appear on the forward slopes of GCW in the cm–dm – wavelengths range. The length of the ripples is about 5–6 mm and decreases down the GCW slope [*Ermakov et al.*, 1986, 2022; *Longuet-Higgins*, 1995], it also decreases with increasing GCW length, so that the ripples are barely visible for GCWs with lengths exceeding 30–35 cm. In our calculations, there were no parasitic ripples on the profile, because of insufficient resolution of the computational grid. GCW with lengths of approximately 0.5 m and longer collapse under sufficiently large amplitudes, forming an ambiguous profile (capsize) and a turbulent “spilling breaker” that “slides” down the slope. It follows from Figure 5 that the normal to the wave surface at crest is directed vertically upward, while in the wave breaking part of the profile the normal is almost horizontal, the elevation of the surface tends to be ambiguous at the forward slope, and a local breaking occurs at this point. The bulge-like structure (and micro-breaking) is also accompanied by the appearance of a downward current within a narrow subsurface layer. It is illustrated by Figure 6, which depicts the vertical velocity profile of GCW on the horizontal section of a wave crest. These sections indicated as dotted lines on Figures 4 and 5. This type of flow dynamics is not observed in the case of relatively small-amplitude waves that are far from breaking, as can be seen in Figure 6. The presence of this downward vertical velocity is likely the cause of the sinking of the film edge below the water surface (see, below).

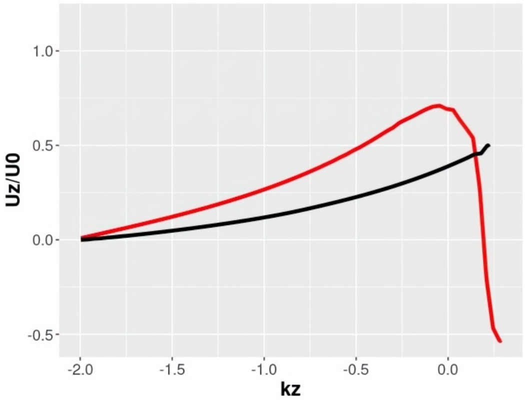

Figure 6. Normalized vertical velocity on the horizontal section (dotted lines on Figures 4 and 5) of a wave crest for a steep GCW (red line) and small amplitude GCW (black line) vs dimensionless depth.

3.2. *Film Dynamics in the Presence of GCW*

3.2.1. Small amplitude GCW

First, experiments were performed with surface waves of small amplitudes ($ka \sim 0.14$–0.18). In this range of steepness values the sinking effect is not observed, and the film actually follows the shape of the wave and remains on the water surface, as shown in Figure 7.

Figure 7. Small amplitude GCW. Blue color corresponds to the water, gray to the air, and yellow to the film.

Figure 7 demonstrates the result of modeling of the small amplitude wave propagation in the presence of a PE film with the elasticity $E_s = 2 \times 10^8$ Pa, located on the surface. It is seen that the film actually follows the wave profile. In the case under consideration, the film length was approximately twice the wavelength, however, qualitatively the effect remained unchanged also at other ratios of the film size to the wavelength of small-amplitude GCW.

3.2.2. Steep GCW.

Below we consider the case where the local wave breaking of steep GCW occurred near the left boundary of the film. The breaking leads to the overflow of water over the film and, as a result, to the immersion of the film under the water surface. This process is depicted in Figure 8.

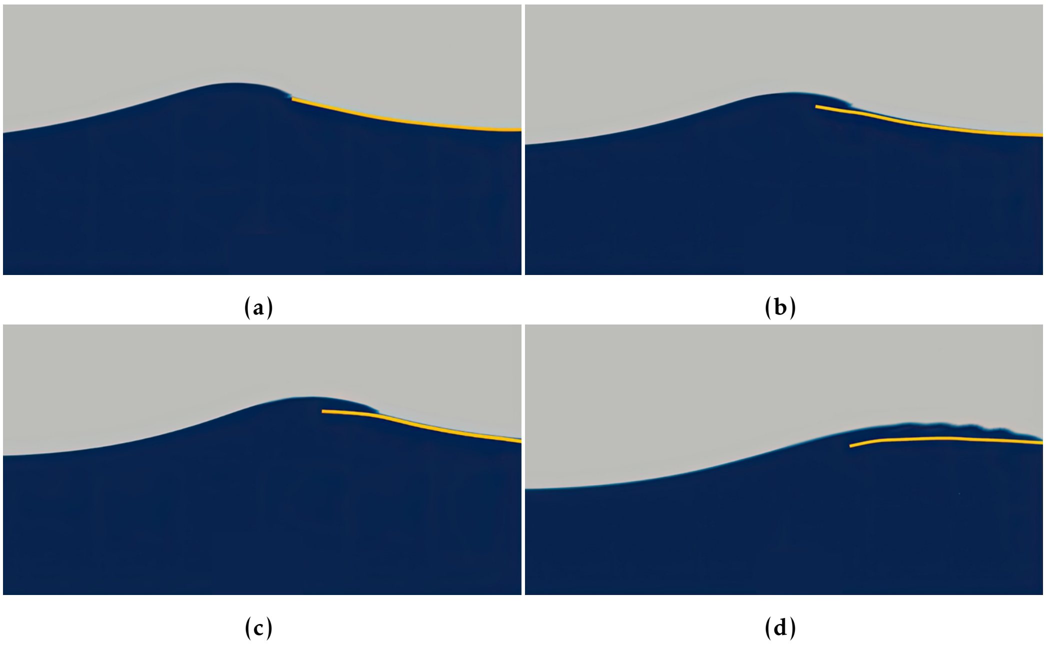

Figure 8. Steep GCW and a highly elastic film (a) $t = 2.97$ s, (b) $t = 3.003$ s, (c) $t = 3.036$ s, (d) $t = 3.102$ s. The elasticity of the film $E_s = 2 \times 10^8$ Pa.

One can see how a steep wave runs into the film and overflows it. Later, the left edge of the film moves from the water surface into the near-surface layer. This is associated with downward vertical velocity at the crest, that is consistent with the vertical velocity profile which is shown in Figure 6.

The subsequent film dynamics depends significantly on the film elasticity. Since the film dynamics in the presence of significant bending due to surface waves can be quite complex, a simplified problem for a small piece of film is considered below. A series of simulations of the dynamics of a small floating film, which size is much smaller than GCW length, were conducted for various surface wave parameters. The PE film length was 4.5 cm, the thickness was 0.4 mm.

To simplify our numerical calculations we supposed the film to be initially submerged due to GCW, and during the simulations, the film immersion depth – h and the wave steepness – ka were varied.

First, we consider a simple case in which there is no surface waves, and the film is located initially at a certain depth. In this case, the film, whose density is slightly lower than that of water, slowly rises to the surface. Figure 9 demonstrates the dynamics of the buoyant film "flotation" – the dependence of the dimensionless vertical coordinate on dimensionless time. The film quickly acquires a nearly constant velocity. The next case is the dynamics of a film starting at $t = 0$ from a certain depth in the presence of surface waves. A comparison of the film dynamics with and without surface waves is shown in Figure 9.

It can be seen that the averaged rate of film rise decreases with time and, having reached a certain level, the film stays at this equilibrium depth. The film vertical averaged

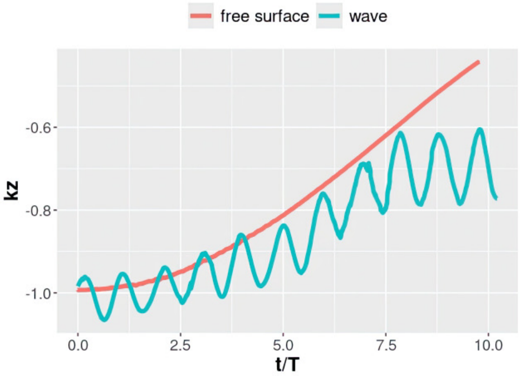

Figure 9. Dimensionless vertical coordinate of the film vs dimensionless time for “no waves” case (red) and with surface waves (blue).

velocity is lower than its velocity in the absence of surface waves. One should note, that following [*Khazanov and Ermakov*, 2025], the periods of the waves, T – wave period, were chosen much smaller than the characteristic time of the film ascent.

4. Discussion

Since a PE film in the presence of surface waves is rising slower than in the “no wave” case (see Figure 9) one can conclude, that some averaged hydrodynamic force **F** arises in the field of orbital wave motions of the liquid particles. This force is directed against the Archimedean force and is responsible for film sinking.

The fast oscillating hydrodynamic force **F**, which arises when the wave orbital flows around a PE film, is determined by the integral of the dynamic components of the stress tensor over the film surface. Due to the high complexity of the flow around the film, this force cannot be described analytically. However, it can be calculated numerically. If we subtract the Archimedean force and the force of gravity from the calculated film acceleration multiplied by its mass $m_f \frac{d^2 z}{dt^2}$ (see, below), only oscillating force acting on the body remains. An example of thus calculated hydrodynamic force **F** for certain wave parameters is shown in Figure 10.

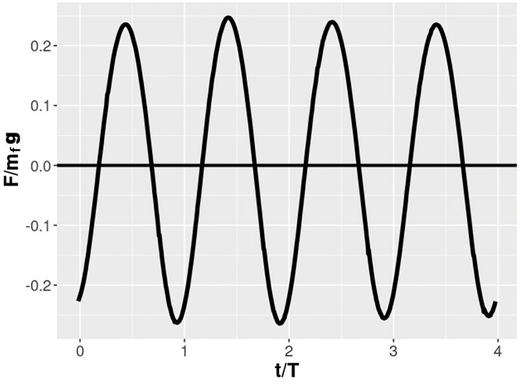

Figure 10. Numerically calculated oscillating vertical component of the normalized hydrodynamic force acting on the film at the depth $kz = -0.84$ due to GCW with the steepness $ka = 0.08$.

If we consider the motion of the film as a whole, without taking into account the change in its shape and describing the vertical position of the film by one coordinate z, then the equation of motion of the film can be written as following,

$$m_f \frac{d^2 z}{dt^2} = g m_f \left(\frac{\rho_w}{\rho_f} - 1 \right) + F. \tag{6}$$

Here ρ_w and ρ_f – water and film densities, m_f – mass of the film, and the first term in the right-hand side of (6) corresponds to the difference between the Archimedes force and gravity.

Representing the film motion as fast oscillating small vibrations of the film due to the hydrodynamic force F and a slowly changing component $Z(t) = \overline{z(t)}$, obtained as a result of averaging the motion over the period of the wave, one can obtain an equation describing the average motion of the film in the form [see, also *Landau and Lifshitz*, 1988]:

$$m_f \frac{d^2 Z}{dt^2} = g m_f \left(\frac{\rho_w}{\rho_f} - 1 \right) - \frac{\partial \overline{F^2}}{\partial Z} \frac{1}{2 m_f \omega^2}, \tag{7}$$

where the overbar denotes averaging over the wave period. The last term represents the average force acting on the film in the surface wave field. Given the exponential decay of wave motion with depth, the average force can be written as $\frac{\overline{F^2} k}{m_f \omega^2}$. This force is directed downwards and causes the film to sink.

Physically, the sinking of the PE film can be explained by the fact that the fast oscillating force causing the film to oscillate in the field of wave orbital motion depends on depth. It is greater during the oscillation phase when the film begins to sink and less when it rises due to the decrease in orbital velocity with depth. Using the calculation of the oscillating force shown in Figure 10, it is easy to estimate the ratio of the averaged force and the buoyancy force, i.e., the ratio of the second term to the first on the right-hand side of (7). For the above-mentioned problem parameters and for a wave with a steepness of $ka = 0.08$ at $kz = -0.84$, the averaged force is approximately 0.25 of the buoyancy force and acts opposite to it, which results in slower initial rising of the film than in the absence of waves. As it follows from Figure 3, when the film floats up, the amplitude of the orbital velocity of the wave increases, and accordingly, both the oscillating and averaged forces increase, which leads to dynamic equilibrium of the film at a certain depth.

The hydrodynamic force depends significantly on the surface wave parameters, particularly its steepness. The dependence of the average force on wave steepness for a fixed ratio of the PE film size to the wavelength is shown in Figure 11. It can be seen that the force has a quadratic dependence on wave steepness. The force itself and its qualitative dependence on other dimensionless parameters of this problem are the subject of further research.

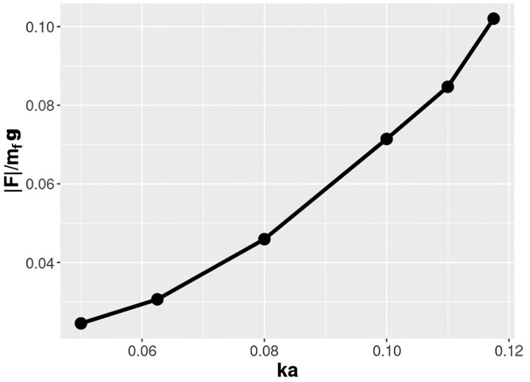

Figure 11. Average force $\frac{\overline{F^2} k}{m_f \omega^2}$ vs wave steepness.

As already mentioned, the dynamics of the film on the water surface depends significantly on the elasticity parameter. Since the elasticity of the film in the calculation above was chosen quite high ($E_s = 2 \times 10^8$ Pa) one can assume that the film could not bend in the collapse zone due to its elasticity, but it can at lower elasticity. To check this assumption the calculations were performed for different values of elasticity, and Figure 12 shows an example of the dynamics of a film with the elasticity less by an order of magnitude, namely for $E_s = 2 \times 10^7$ Pa.

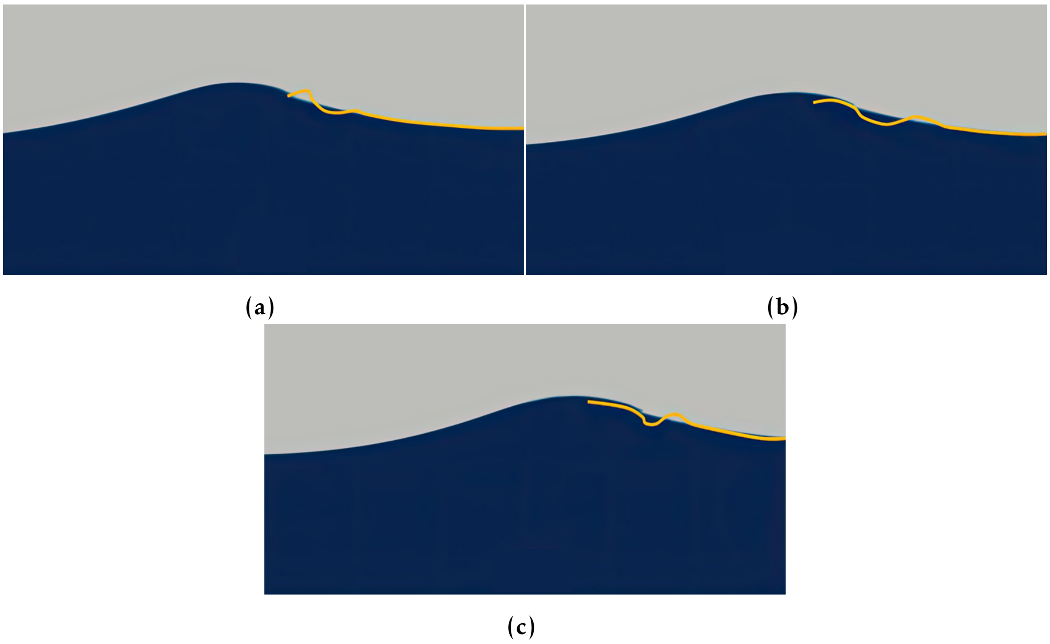

Figure 12. Steep GCW and a low elastic film (a) $t = 2.97$, (b) $t = 3.003$, (c) $t = 3.036$. Blue color corresponds to the water, gray to the air, and yellow to the film. Film elasticity: $E_s = 2 \times 10^7$ Pa.

A film with lower elasticity is characterized by significantly greater bending deformations in the area of micro-breaking of the GCW. Such deformations are less likely to cause the film to "dive" under the surface wave, resulting in a delay in the film immersion into the water surface layer. It is evident that the elasticity parameter plays a crucial role in the dynamics of the film on the water surface, and further research is needed to understand its impact on the sinking process.

5. Conclusions

Numerical simulations have shown that at low amplitudes of surface waves, a floating polyethylene film located on the surface of the water-air interface oscillates along with the wave and follows its shape.

It has been revealed that for a highly nonlinear GCW with a bulge structure near the crest (micro-breaking), there is an "overflow" of water over the film with the downward vertical velocity at the crest causing subsequent immersion of its edge into the near-surface layer of water. This movement then spreads throughout the film and gradually causes the film to sink along its entire length. It has also been shown that a buoyant PE film sank below the water surface rises slower in the presence of GCW than in the "no wave" case or even continues to sink to a certain equilibrium depth. The explanation of the film immersion effect is based on the hypothesis that an averaged hydrodynamic force arises in the field of orbital wave motions of the liquid particles. This force is directed against the Archimedean force and is responsible for film sinking. It is shown that this force depends significantly on the steepness of the wave and an estimate of the magnitude of this force is given.

Acknowledgments. This work was supported by the Russian Science Foundation (Project No 23-17-00167). The data that support the findings of this study are available from the corresponding author upon reasonable request.

References

Andrady A. L. Microplastics in the marine environment // Marine Pollution Bulletin. — 2011. — Vol. 62, no. 8. — P. 1596–1605. — https://doi.org/10.1016/j.marpolbul.2011.05.030.

Arii M., Koiwa M. and Aoki Yo. Applicability of SAR to Marine Debris Surveillance After the Great East Japan Earthquake // IEEE Journal of Selected Topics in Applied Earth Observations and Remote Sensing. — 2014. — Vol. 7, no. 5. — P. 1729–1744. — https://doi.org/10.1109/jstars.2014.2308550.

Brown S. A., Xien N., Hann M. R., et al. Investigation of wave-driven hydroelastic interactions using numerical and physical modelling approaches // Applied Ocean Research. — 2022. — Vol. 129. — P. 103363. — https://doi.org/10.1016/j.apor.2022.103363.

Cardiff P., Karač A., De Jaeger P., et al. An open-source finite volume toolbox for solid mechanics and fluid-solid interaction simulations. — arXiv, 2018. — https://doi.org/10.48550/ARXIV.1808.10736.

Chubarenko I., Esiukova E., Khatmullina L., et al. From macro to micro, from patchy to uniform: Analyzing plastic contamination along and across a sandy tide-less coast // Marine Pollution Bulletin. — 2020. — Vol. 156. — P. 111198. — https://doi.org/10.1016/j.marpolbul.2020.111198.

Ciarlet P. G. Mathematical Elasticity. Volume I, Three-Dimensional Elasticity Studies in Mathematics and its Applications. — Amsterdam : Elsevier Science Publishers B.V., 1988. — 451 p. — https://doi.org/10.1007/BF00046568.

Cózar A., Echevarría F., González-Gordillo J. I., et al. Plastic debris in the open ocean // Proceedings of the National Academy of Sciences. — 2014. — Vol. 111, no. 28. — P. 10239–10244. — https://doi.org/10.1073/pnas.1314705111.

Davaasuren N., Marino A., Boardman C., et al. Detecting Microplastics Pollution in World Oceans Using Sar Remote Sensing // IGARSS 2018 - 2018 IEEE International Geoscience and Remote Sensing Symposium. — IEEE, 2018. — P. 938–941. — https://doi.org/10.1109/igarss.2018.8517281.

Dean R. G. and Dalrymple R. Water wave mechanics for engineers and scientists. — World Scientific, 1991. — 353 p.

Donea J., Huerta A., Ponthot J.-Ph., et al. Arbitrary Lagrangian-Eulerian Methods // Encyclopedia of Computational Mechanics. — Wiley, 2004. — P. 413–437. — https://doi.org/10.1002/0470091355.ecm009.

Duncan J. H. Spilling breakers // Annual Review of Fluid Mechanics. — 2001. — Vol. 33, no. 1. — P. 519–547. — https://doi.org/10.1146/annurev.fluid.33.1.519.

Ermakov S. A., Dobrokhotov V. A. and Sergievskaya I. A. Laboratory studies of radar scattering from surface waves propagating over a vertical plastic film submerged in water // Sovremennye problemy distantsionnogo zondirovaniya Zemli iz kosmosa. — 2024. — Vol. 21, no. 6. — P. 320–330. — https://doi.org/10.21046/2070-7401-2024-21-6-320-330. — (In Russian).

Ermakov S. A. and Khazanov G. E. Resonance damping of gravity-capillary waves on water covered with a visco-elastic film of finite thickness: A reappraisal // Physics of Fluids. — 2022. — Vol. 34, no. 9. — https://doi.org/10.1063/5.0103110.

Ermakov S. A., Ruvinsky K. D., Salashin S. G., et al. Experimental investigation of the generation of capillary-gravity ripples by strongly nonlinear waves on the surface of a deep fluid // Izvestiya of the Academy of Sciences of the USSR. Atmospheric and Oceanic Physics. — 1986. — Vol. 22. — P. 835.

Ermakov S. A., Sergievskaya I. A., Dobrokhotov V. A., et al. Wave Tank Study of Steep Gravity-Capillary Waves and Their Role in Ka-Band Radar Backscatter // IEEE Transactions on Geoscience and Remote Sensing. — 2022. — Vol. 60. — P. 1–12. — https://doi.org/10.1109/tgrs.2021.3086627.

Evans M. C. and Ruf C. S. Toward the Detection and Imaging of Ocean Microplastics With a Spaceborne Radar // IEEE Transactions on Geoscience and Remote Sensing. — 2022. — Vol. 60. — P. 1–9. — https://doi.org/10.1109/tgrs.2021.3081691.

Forsberg P. L., Sous D., Stocchino A., et al. Behaviour of plastic litter in nearshore waters: First insights from wind and wave laboratory experiments // Marine Pollution Bulletin. — 2020. — Vol. 153. — P. 111023. — https://doi.org/10.1016/j.marpolbul.2020.111023.

Harrison J. P., Hoellein T. J., Sapp M., et al. Microplastic-Associated Biofilms: A Comparison of Freshwater and Marine Environments // Freshwater Microplastics. Vol. 58. — Cham, Switzerland : Springer International Publishing, 2018. — P. 181–201. — https://doi.org/10.1007/978-3-319-61615-5_9.

Higuera P., Lara J. L. and Losada I. J. Realistic wave generation and active wave absorption for Navier-Stokes models // Coastal Engineering. — 2013. — Vol. 71. — P. 102–118. — https://doi.org/10.1016/j.coastaleng.2012.07.002.

Hron J. and Turek S. A Monolithic FEM/Multigrid Solver for an ALE Formulation of Fluid-Structure Interaction with Applications in Biomechanics // Fluid-Structure Interaction. — Springer Berlin Heidelberg, 2006. — P. 146–170. — https://doi.org/10.1007/3-540-34596-5_7.

Hu C. Remote detection of marine debris using satellite observations in the visible and near infrared spectral range: Challenges and potentials // Remote Sensing of Environment. — 2021. — Vol. 259. — P. 112414. — https://doi.org/10.1016/j.rse.2021.112414.

Jasak H. Error analysis and estimation for the finite volume method with applications to fluid flows. PhD thesis. — Department of Mechanical Engineering Imperial College of Science, Technology, Medicine, 1996.

Khazanov G. E. and Ermakov S. A. Numerical Modeling of a Floating Polyethylene Film Dynamics in the Field of Surface Waves // Fundamental and Applied Hydrophysics. — 2025. — Vol. 18, no. 2. — P. 68–82. — https://doi.org/10.59887/2073-6673.2025.18(2)-5. — (In Russian).

Kukulka T., Proskurowski G., Moret-Ferguson S., et al. The effect of wind mixing on the vertical distribution of buoyant plastic debris // Geophysical Research Letters. — 2012. — Vol. 39, no. 7. — P. 1–6. — https://doi.org/10.1029/2012gl051116.

Landau L. D. and Lifshitz E. M. Theoretical Physics: Vol. I. Mechanics. — Nauka, 1988. — 216 p. — (In Russian).

Longuet-Higgins M. S. Parasitic capillary waves: a direct calculation // Journal of Fluid Mechanics. — 1995. — Vol. 301. — P. 79–107. — https://doi.org/10.1017/s0022112095003818.

Phillips O. M. The dynamics of the upper ocean. — 2nd. — Cambridge : Cambridge University Press, 1977. — 336 p.

Qiao H. and Duncan J. Gentle spilling breakers: crest flow-field evolution // Journal of Fluid Mechanics. — 2001. — Vol. 439. — P. 57–85. — https://doi.org/10.1017/s0022112001004207.

Rapp R. J. and Melville W. K. Laboratory measurements of deep-water breaking waves // Philosophical Transactions of the Royal Society of London. Series A, Mathematical and Physical Sciences. — 1990. — Vol. 331, no. 1622. — P. 735–800. — https://doi.org/10.1098/rsta.1990.0098.

Sapozhnikov P. V., Kalinina O. Y. and Vostokov S. V. Microplaston artificial polymers in the Miass River and Lake Turgoyak (Southern Urals, Russia) in the early stages of colonisation // South of Russia: ecology, development. — 2023. — Vol. 18, no. 3. — P. 133–143. — https://doi.org/10.18470/1992-1098-2023-3-133-143. — (In Russian).

Simpson M. D., Marino A., Maagt P. de, et al. Monitoring of Plastic Islands in River Environment Using Sentinel-1 SAR Data // Remote Sensing. — 2022. — Vol. 14, no. 18. — P. 4473. — https://doi.org/10.3390/rs14184473.

Simpson M. D., Marino A., Maagt P. de, et al. Investigating the Backscatter of Marine Plastic Litter Using a C- and X-Band Ground Radar, during a Measurement Campaign in Deltares // Remote Sensing. — 2023. — Vol. 15, no. 6. — P. 1654. — https://doi.org/10.3390/rs15061654.

Smith I. L., Stanton T. and Law A. Plastic habitats: Algal biofilms on photic and aphotic plastics // Journal of Hazardous Materials Letters. — 2021. — Vol. 2. — P. 100038. — https://doi.org/10.1016/j.hazl.2021.100038.

Suaria G., Cappa P., Perold V., et al. Abundance and composition of small floating plastics in the eastern and southern sectors of the Atlantic Ocean // Marine Pollution Bulletin. — 2023. — Vol. 193. — P. 115109. — https://doi.org/10.1016/j.marpolbul.2023.115109.

Sun Y., Bakker T., Ruf C., et al. Effects of microplastics and surfactants on surface roughness of water waves // Scientific Reports. — 2023. — Vol. 13, no. 1. — https://doi.org/10.1038/s41598-023-29088-9.

Tezduyar T. E., Takizawa K., Moorman C., et al. Space-time finite element computation of complex fluid-structure interactions // International Journal for Numerical Methods in Fluids. — 2010. — Vol. 64, no. 10–12. — P. 1201–1218. — https://doi.org/10.1002/fld.2221.

Thomas P. D. and Lombard C. K. Geometric Conservation Law and Its Application to Flow Computations on Moving Grids // AIAA Journal. — 1979. — Vol. 17, no. 10. — P. 1030–1037. — https://doi.org/10.2514/3.61273.

Tuković Ž. and Jasak H. A moving mesh finite volume interface tracking method for surface tension dominated interfacial fluid flow // Computers & Fluids. — 2012. — Vol. 55. — P. 70–84. — https://doi.org/10.1016/j.compfluid.2011.11.003.

Tuković Ž., Karač A., Cardiff P., et al. OpenFOAM Finite Volume Solver for Fluid-Solid Interaction // Transactions of FAMENA. — 2018. — Vol. 42, no. 3. — P. 1–31. — https://doi.org/10.21278/tof.42301.

Vodeneeva E., Pichugina Yu., Zhurova D., et al. Epiplastic Algal Communities on Different Types of Polymers in Freshwater Bodies: A Short-Term Experiment in Karst Lakes // Water. — 2024. — Vol. 16, no. 22. — P. 3288. — https://doi.org/10.3390/w16223288.

Widlund O. Iterative substructuring methods: algorithms and theory for elliptic problems in the plane // First International Symposium on Domain Decomposition Methods for Partial Differential Equations. — Paris, France : SIAM, 1988. — P. 113–128.